SPARSE INFERENCE OF NONLINEAR LABORATORY EARTHQUAKE DYNAMICS

JESSICA HU, ARYAN RAJ, AND SHIJIE ZHANG

Abstract. The frictional state of faults plays a fundamental role in earthquake nucleation and recurrence. Laboratory earthquake ("labquake") experiments provide controlled conditions for investigating stick-slip dynamics, yielding high-resolution data on shear stress, gouge evolution, and acoustic emissions (AEs). While prior work has shown that AEs can be used to forecast failure times with machine learning, such models provide limited physical interpretability and require large datasets. Moreover, mechanistically discovering the governing equations of labquake systems remains difficult due to their nonlinear and stochastic nature. In contrast, data-driven inference of governing equations offers a transparent and flexible pathway to uncover the physical rules behind fault stress evolution. Here, we introduce a novel stochastic Bayesian inference framework to systematically analyze labquake frictional dynamics. We infer governing stochastic differential equations (SDEs) with inhomogeneous Poisson processes, incorporating both microslip and major slip failures. Our results reveal that the growth function for fault stress follows a nonlinear hyperbolic sine relation with respect to the frictional state, inferred using the ADAM-SINDy framework, which combines sparse nonlinear model discovery with Adam optimization. This approach provides physically interpretable governing equations, bridging the gap between phenomenological labquake data and theoretical friction laws. More broadly, our methodology demonstrates how stochastic inference can mechanistically uncover governing equations in complex natural systems such as landslides and fracture mechanics.

Keywords: dynamical systems, system identification, stochastic differential equations, laboratory earthquakes

Date: January 18, 2026.

Contents

1. Introduction

Earthquakes are the result of a sudden release of accumulated stress along a geological fault. Friction generated by the interactions between rock granules in a fault dictate the nucleation, propagation, and cessation of seismic events. Thus, understanding the gradual build and release of frictional stress in faults is instrumental for earthquake prediction. However, directly observing fault friction and its temporal evolution remains challenging due to a lack of data. Although large-scale computer simulations based on plate tectonics can provide estimates of fault stress and frictional state, these estimates often fail to capture the nuances of tectonic phenomena [50, 54]. Until recently, even state-of-the-art computer models were unable to accurately predict actual fault behavior [34, 53].

Due to the difficulties associated with gathering data from real-world seismic events, laboratory earthquake ("labquake") experiments have been explored as a more feasible alternative [19, 24, 28, 35, 36, 37, 47], leading to significant progress in our understanding of frictional processes [3, 8, 26, 40, 45]. Labquake experiments have emerged as powerful tools for investigating fault mechanics under controlled conditions. The stick-slip behavior exhibited by geological faults can be reproduced in a laboratory setting through an apparatus consisting of granular gouge layers, put under a constant normal load and shear velocity, depicted in Figure 1 (A). These experiments produce highly detailed time-series data on shear stress, normal stress, gouge layer thickness,

and shear displacement, as well as acoustic emissions (AEs), which serve as proxies for microseismic activity within the fault zone [35, 36, 37].

Recent studies have demonstrated the predictive power of AEs in estimating time-to-failure (TTF) and frictional states of labquakes, achieving high accuracy using machine learning (ML) models [36, 37]. However, while approaches based on ML models have advanced predictive capabilities, they provide little insight into the underlying physical laws behind the evolution of frictional states, black-boxing labquakes. Thus, the challenge of mathematically modeling fault stress and behavior over time remains open.

We propose the method of modeling labquake frictional states as a nonlinear dynamical system. We are motivated by previous literature's exploration of this method, applied to a diversity of natural systems, such as DNA sequence evolution [46], bacterial population growth [1], and cell division [52]. Past algorithms, such as the pioneering Sparse Identification of Nonlinear Dynamics (SINDy) [9], model dynamical systems with ordinary differential equations (ODEs) and infer these equations through sparse regression with a sequential thresholded least-squares approach. Extensions of the SINDy approach have explored the inference of governing partial differential equations (PDEs) [38] and ODEs of certain nonlinear forms, such as rational fractions [22].

However, the stochasticity of labquakes, seen in time evolution dynamics' qualitative resemblance to a Poisson process [17], means that past SINDy algorithms are unable to address the intricacies of frictional state evolution. Instead, recent advances in stochastic modeling have introduced inference techniques that enable the direct identification of governing stochastic differential equations (SDEs) from time-series data [52, 9]. Here, we propose an approach for labquake analysis using SDEs to describe fault stress evolution. We employ a novel Bayesian inference-derived probabilistic model based on SDEs, combined with an ADAM-SINDy framework to interpret frictional growth, in order to gain insights on labquake frictional states' evolution.

2. Methods

2.1. **Labquake Friction Physics.** The study of friction laws in rock mechanics and fault dynamics has a precedent from as far back as the second half of the 20th century, with early laboratory experiments providing foundational insights into fault slip behavior [5, 6, 7, 11, 10, 13, 15, 18, 20, 24, 25, 29, 44, 42, 43, 48, 49].

A major advancement in frictional theory came with the development of rate-and-state-dependent friction laws, which account for the dependence of frictional strength on both slip velocity and the evolving state of contact asperities [14, 31, 33, 32, 39, 41]. These laws introduced a state variable, θ, which describes the time-dependent evolution of friction due to contact aging effects. The general form of the rate-and-state friction equation is given by the following:

$$\mu = \mu_0 + a \ln\left(\frac{V}{V_0}\right) + b \ln\left(\frac{V_0 \theta}{D_c}\right), \tag{2.1}$$

where μ_0 is the reference friction coefficient, V is the slip velocity, V_0 is a reference velocity, a and b are empirical constants, D_c is the characteristic slip distance over which friction evolves, and θ is a governing state variable that grows over time, dictating the time-evolution behavior of μ.

2.2. **Stochastic Differential Equations Inference.** Of particular interest to us is the fact that labquakes are characterized by stochasticity [17], which motivates our modeling of fault behavior with SDEs. We apply a data-driven approach [52] to inferring SDEs.

A classic SDE with a discrete Poisson process is of the following form:

$$ds_t = g(s_t)dt - h(s_{t-})d\mathscr{N}_t(\lambda_t), \tag{2.2}$$

where at some time t, the state variable has value s_t. The deterministic drift function $g(s_t)$, while the jump during Poisson event is modeled by function $h(s_{t-})$. The Poisson process $\mathscr{N}_t$ is dependent on the Poisson intensity λ_t, which may vary over time and can also depend on the state variable s_t. More generally speaking, the intensity λ_t may differ across scenarios, reflecting different system dynamics. Here, we consider the intensity to depend on the current state and the state before: $\lambda_t = \lambda(s_t, s_t^*)$, where s_t^* refers to the previous state. In the Poisson process, we consider $d\mathscr{N}_t = 1$ when an event occurs; otherwise, $d\mathscr{N}_t = 0$.

For the simplest example, we consider the deterministic drift function $g(s_t)$ and the jump function $h(s_{t-})$ to be linear. Then, the coefficients g_i and h_i may be found through a linear regression.

To ensure that $\lambda_t = \lambda(s_t, s_t^*)$ is always positive, we represent $\ln \lambda$ as the following:

$$\ln \lambda(s_t, s_t^*) = \sum_{i,j} \mathbf{w}_{ij}\theta_i(s_t)\theta_j(s_t^*). \tag{2.3}$$

Here, θ_i and θ_j are orthogonal polynomials constructed using the Gram-Schmidt procedure [4] and weighted by $\mathbf{w}_{ij}$. We then proceed with maximum likelihood estimation on $\hat{\mathbf{w}}$ to find the most probable values. In particular, we aim to find $P(\mathbf{w}|s_t)$, which by Bayes' theorem is

$$P(\mathbf{w}|s_t) = \frac{P(s_t|\mathbf{w})P(\mathbf{w})}{P(s_t)}.$$

We may use properties of the inhomogeneous Poisson process $\mathscr{N}_t$ to find $P(s_t|\mathbf{w})$ and sparse Bayesian inference to estimate $P(\mathbf{w})$. (Details in Appendix, Section 7.1). Ultimately, we may obtain $\lambda(s_t, s_t^*)$ from Equation 2.3, which informs us of how the Poisson intensity depends on both the current state and the state before.

Similar to the sequential thresholding least squares method introduced by the original SINDy paper [9], we sequentially threshold coefficients $\hat{\mathbf{w}}$ to create a set of candidate models for the original SDE (2.2). After doing so, we may use the Bayesian Information Criterion (BIC) to select the most parsimonious one. (Details in Appendix, Section 7.1).

2.3. **Application of SDE Inference to Labquakes.** We adopt the above SDE inference framework and apply it to inferring labquake frictional dynamics. As noted in prior literature, the frictional state μ follows a characteristic stick-slip cycle, where shear stress accumulates gradually before experiencing abrupt stress releases due to slip events [36, 37]. In addition, shear microfailures, which we refer to as "microslips," often precede major slip events, particularly in experiments with low normal stresses [19]. Thus, drops in the friction state parameter μ exhibit a strong dichotomy between major ($\Delta\mu > 0.04$) and micro ($\Delta\mu < 0.04$) slip events, as seen in Figure 6 of Appendix, Section 7.2.

As a result, the basic SDE inference technique, which incorporates only one Poisson drop process, cannot be generalized to model all laboratory earthquake frictional trajectories. Small precursor slips occur at varying intervals leading up to a major slip event, implying a structured relationship between minor and major stress drops, which are evident in Figure 1 (B).

Thus, we introduce a modeling approach that incorporates two separate Poisson processes with nonlinear memory of past states. Recall that the standard SDE inference framework aims to infer an equation of the form

$$d\mu_t = g(\mu_t)dt - h(\mu_{t-})d\mathscr{N}_t(\lambda_t),$$

where the frictional coefficient μ_t evolves under a deterministic function $g(\mu_t)$ and experiences discontinuous stress drops governed by a stochastic Poisson process $\mathscr{N}_t(\lambda_t)$ [52]. To extend this method to encompass the effects of small and large faulting, we introduce two distinct rate functions, λ^m and λ^M, corresponding to microslips and major slip events, respectively. We assume that the governing equation takes the form

$$d\mu_t = g(\mu_t)dt - h^m(\mu_{t-})d\mathscr{N}_t(\lambda_t^m) - h^M(\mu_{t-})d\mathscr{N}_t(\lambda_t^M),$$

where $g(\mu_t)$ describes the deterministic accumulation of friction while the Poisson-driven terms represent discrete stress drops due to microslip and major slip events. The event rates λ^m and λ^M are history-dependent functions of the past fault state.

We use the experimental trajectories of μ_t as input data and apply the SDE inference framework of Section 2.2 to infer the functions $g(\mu_t)$, $h^m(\mu_{t-})$, $h^M(\mu_{t-})$, and $\lambda^m(\mu_t, \mu_t^*)$, $\lambda^M(\mu_t, \mu_t^*)$, where, μ_t^* refers to the previous frictional state. These ideas are visually summarized in Figure 1 (C) and (D). The ADAM-SINDy approach, which we explain further in Section 3.4, is used to infer $g(\mu_t)$, while the slip functions h^m and h^M are extracted from the empirical distribution of stress drops, categorized into microslip and major slip events.

For our preliminary analysis, we confine our attention to the case where both λ^m and λ^M only depend on one-generational predecessor state memory; i.e., the current frictional state depends only on the frictional state immediately prior to the last major slip event.

To infer these slip rates, we construct a basis representation using Chebyshev polynomials and apply Gram-Schmidt orthogonalization to generate a reduced basis set. The

basis representation allows us to express the slip rate functions λ^m and λ^M in terms of an optimal sparse combination of basis functions. The inferred functions are obtained through a sparse Bayesian optimization (maximum likelihood estimation) procedure, where an iterative algorithm prunes irrelevant terms to enforce parsimony. This procedure is applied separately for small and large slip events, leading to distinct functional forms for the two regimes. Once the functions are inferred, the model with the highest BIC score is chosen as the final inferred equation.

3. Results

We now proceed to outline the results obtained from our attempts to infer the governing equations that describe the evolution of the frictional state μ, as discussed in Section 2.3 and Appendix, Section 7.1. This inference relies on the analysis of shear stress time-series data collected from controlled laboratory experiments simulating earthquake-like stick-slip behavior. Specifically, we used data from a set of experiments conducted under varying normal stress conditions.

For the normal stresses of 4 MPa, 5 MPa, 6 MPa, 7 MPa, and 8 MPa, the shear stress data were extracted from a single labquake experiment, labeled `p2394` from data repository [23]. These runs simulate fault gouge behavior under relatively low confining pressures and offer well-resolved stick-slip cycles that include both major and minor stress drops. The time-series data for these experiments were sampled at intervals of $dt = 0.1\,\mathrm{s}$, which provides a relatively coarse but still sufficiently informative view of the stress evolution, especially at slower slip rates.

For higher normal stresses, specifically 9 MPa, 10 MPa, 11 MPa, and 13 MPa, we relied on a different set of labquake experiments: `p4346`, `p4347`, `p4348`, and `p4350`, respectively. These experiments were conducted under stronger confining loads and, as expected, exhibited qualitatively different stress-time behavior, including more abrupt and isolated slip events. The data for these experiments were recorded with a much finer temporal resolution of $dt = 0.001\,\mathrm{s}$, enabling detailed observation of high-frequency stress fluctuations. This high-resolution sampling is crucial for capturing the sharp transitions that characterize rapid failure events at high normal stress.

3.1. Data Processing.

As established in prior labquake literature, the frictional state μ tends to follow a distinctive stick-slip trajectory: shear stress accumulates gradually over time, forming a rising slope, until a sudden release occurs in the form of a stress drop corresponding to a slip event [36, 37]. These stress drops may be large, corresponding to full-scale slip events (akin to small earthquakes), or relatively minor, corresponding to microslip events. Accordingly, the goal of our data processing pipeline was to clean the raw time-series data and accurately identify the locations of these slip events.

Our first step was denoising the data. We applied a total variation (TV) denoising algorithm to the full dataset across all normal stress levels. This method is well-suited to preserving discontinuities (such as those from sudden stress drops) while filtering out

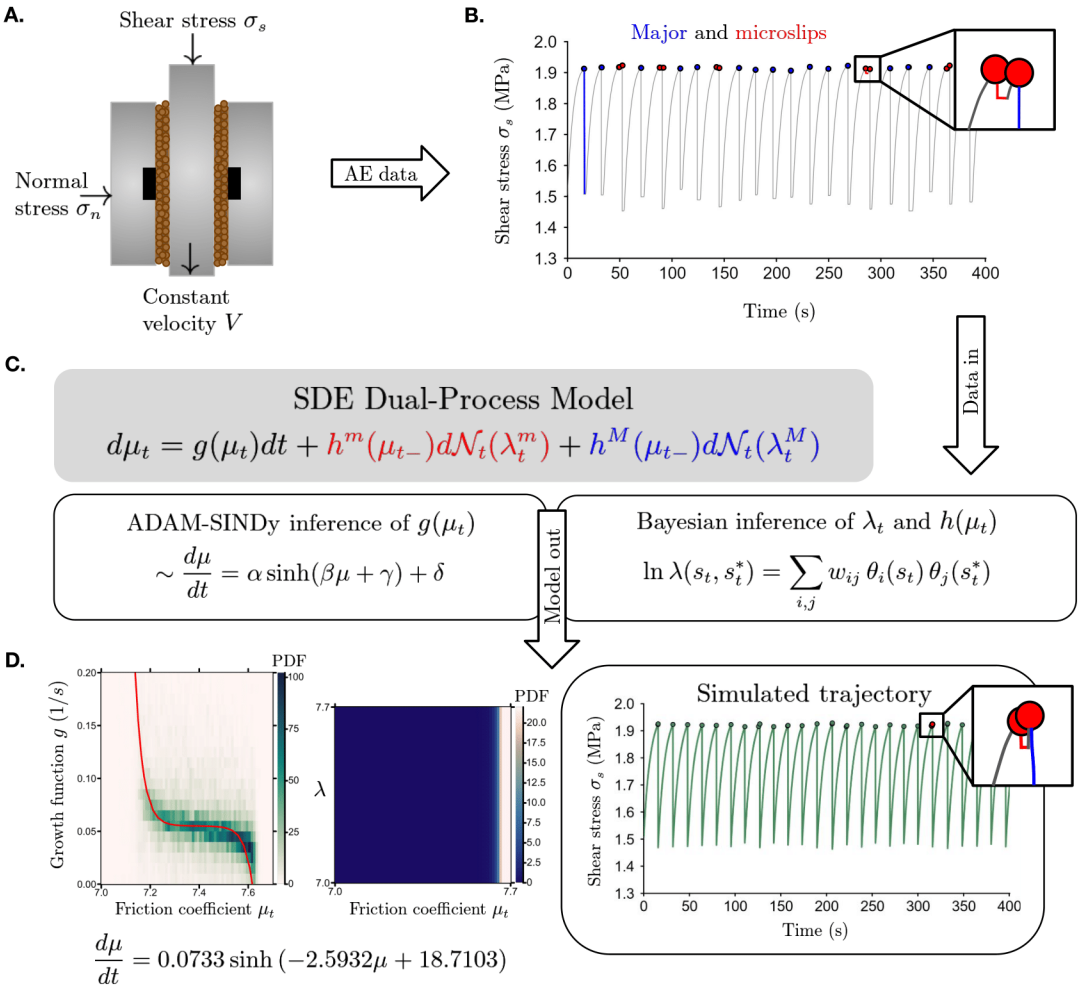

Figure 1. (A) Visualization of the apparatus used to generate labquakes and collect acoustic emission (AE) data. The apparatus is comprised of metal sheets and layers of glass beads that generate friction due to a shear stress and a normal stress. (B) Shear stress trajectory, created with experimental data from Chris Marone's experiment `p2394` [23] at 5 MPa. At low normal stresses (2-8 MPa), both major slips, denoted in blue, and microslips, in red, are exhibited. At high normal stresses (9-13 MPa), only major slips are exhibited. (C) Dual-process model for labquake friction at low normal stresses, based on a stochastic differential equation (SDE). Major and microslips arrive according to two Poisson processes at different rates h^M and h^m, respectively. The growth function g is empirically and theoretically determined to follow a sinh relation, whose coefficients are calculated through an ADAM-SINDy inference. The Poisson rates λ^M and λ^m are determined through a Bayesian inference. (D) Experimental results from the model for experiment `p2394` at 11 MPa, including the inference for g and λ and the simulated trajectory of the shear stress.

high-frequency noise. For the low- to moderate-stress experiments (2–8 MPa), which were drawn from experiment `p2394`. After denoising, we identified every local maximum in the shear stress trajectory as the beginning of a slip, with the slip ending at the next

local minimum. This approach allowed us to capture not only the major drops in μ, but also the smaller precursory drops that characterize microslip behavior. These small stress reductions are of particular interest, as prior studies have shown that they may precede larger events and serve as early indicators of impending failure [19].

In contrast, the data from the high-stress experiments (9–13 MPa) required a different strategy. The much finer time resolution ($dt = 0.001\,\mathrm{s}$) in these datasets meant that standard peak-detection methods could erroneously identify noise or small fluctuations as slip events. Furthermore, upon visual inspection, we observed that these experiments did not exhibit microslips; instead, the stress trajectories featured isolated, abrupt, and distinctly large drops in μ corresponding to major failures. Therefore, we modified our approach for these cases: we first removed all intermediate data points that lay within a large slip event (i.e., between the onset and termination of a steep drop), thereby simplifying the stress profile. We then applied an amplitude-based threshold to eliminate any remaining small drops that might still be detected as peaks due to numerical fluctuations or rounding artifacts. This ensured that only significantly large, physically meaningful slips were marked and retained in the dataset.

By tailoring our data processing methods to the properties of each experimental regime, we were able to cleanly separate buildup phases from slip phases and prepare the data for stochastic inference using the models described in later sections.

3.2. **Results from Inference.** Using the stochastic modeling framework outlined in Section 2.3, we inferred governing equations for labquake friction under a range of normal stresses. For low to moderate normal stresses (2–8 MPa), we observed a rich stick-slip behavior with both microslip and major slip events. Thus, we employed a dual-Poisson stochastic model, with separate intensity functions λ^m and λ^M to represent the occurrence of microslips and major slips, respectively. For higher normal stresses (9–13 MPa), however, microslips were effectively absent, and we used a simplified single-Poisson model with only λ^M governing major slip events.

Across all conditions, the growth function $g(\mu_t)$ exhibited a consistent hyperbolic sine structure, as discussed in Appendix, Section 7.1. The inferred g captured the nonlinear build-up of friction over time, with growth rates increasing rapidly at higher μ_t values.

A key challenge arose when inferring the major slip intensity function $\lambda^M(\mu_t, \mu_t^*)$, particularly for the 10 MPa case. Using sparse Bayesian inference, we consistently observed that the inferred λ^M showed no dependency on memory μ_t^*, effectively collapsing to a one-variable function $\lambda^M(\mu_t)$. This result was surprising, as physical intuition and prior studies suggest that the history of fault friction plays a critical role in slip nucleation.

To investigate further, we applied ridge regression to the same Chebyshev-polynomial basis representation. Unlike the sparsity-driven Bayesian approach, ridge regression penalizes all coefficients uniformly, allowing for weaker but still significant dependencies to be preserved. This adjustment revealed a clear two-variable structure in $\lambda^M(\mu_t, \mu_t^*)$, demonstrating that memory effects, though subtle, do exist and can be recovered with

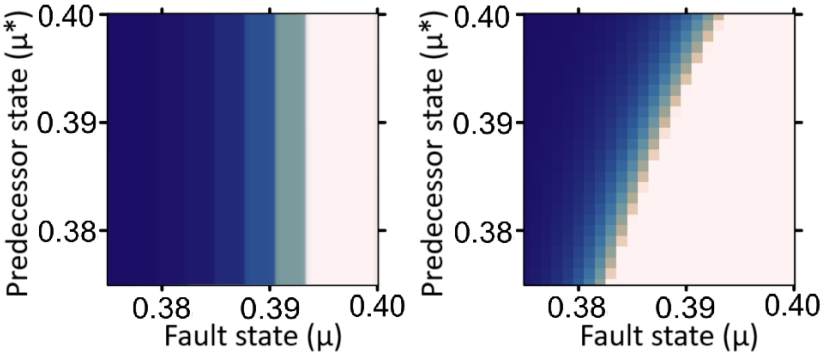

Figure 2. Comparison of inferred major slip rate $\ln \lambda^M(\mu_t, \mu_t^*)$ for the 10 MPa case. The x-axis of each graph represents μ_t and the y-axis of each graph represents μ_t^*. Bluer points represent lower values of $\lambda^M(\mu_t, \mu_t^*)$. Left: Bayesian sparse inference shows that there is no memory effect. Right: Ridge regression reveals clear dependence on both current and past frictional states.

appropriate regularization, as shown in Figure 2. We therefore proceed with ridge regression to preserve these subtleties.

3.3. **Varying Normal Stresses.** To assess the generalizability and robustness of our stochastic modeling framework, we analyzed labquake experiments conducted at a wide range of normal stress values, from 2 MPa to 13 MPa. The behavior of shear stress over time and the statistical distribution of slip sizes varied substantially across this range, revealing key differences in failure dynamics that our model aims to capture.

At lower normal stresses (2–8 MPa), the system exhibited a rich spectrum of behavior characterized by numerous small stress drops interspersed with larger ones. These experiments, drawn from dataset `p2394`, featured the hallmark of stick-slip friction: gradual accumulation of shear stress followed by intermittent releases, often with precursory microslip events. Consequently, we employed a dual-Poisson stochastic model to capture this dynamic, with one Poisson process governing small drops and another governing large ones.

At higher normal stresses (9–13 MPa), the behavior changes significantly. Experiments in this regime—such as `p4346` for 9 MPa—display infrequent but abrupt and large shear failures, with microslips effectively absent. As a result, we modeled these cases using a single-Poisson process focused exclusively on major slips. Despite this simplification, the model was still able to accurately replicate the core dynamics of failure.

To evaluate the validity of our inferred models across these regimes, we compared the original experimental shear stress trajectories and slip size histograms with their simulated and resimulated counterparts. Figure 3 presents a unified visual summary for two representative cases: 5 MPa (low stress) and 9 MPa (high stress). The top two panels correspond to the 5 MPa condition, showing both the shear stress trajectory and slip size histogram. The bottom two panels show the same for the 9 MPa condition.

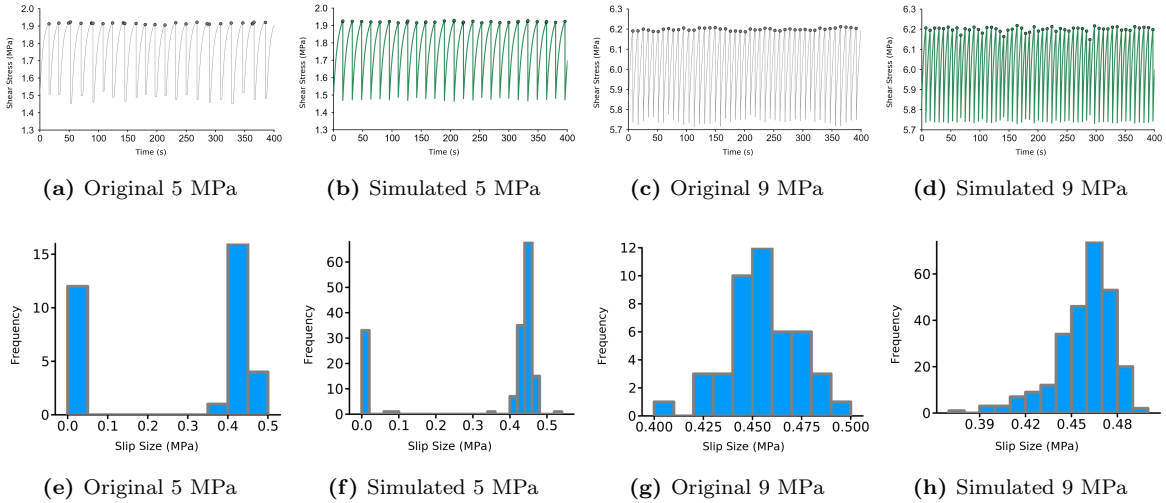

(a) Original 5 MPa **(b)** Simulated 5 MPa **(c)** Original 9 MPa **(d)** Simulated 9 MPa

(e) Original 5 MPa **(f)** Simulated 5 MPa **(g)** Original 9 MPa **(h)** Simulated 9 MPa

Figure 3. Combined comparison of experimental and simulated results. **(a–d):** Shear stress trajectories for 5 MPa and 9 MPa, modeled with dual- and single-Poisson processes, respectively. **(e–h):** Slip size histograms for 5 MPa and 9 MPa. The modeling framework accurately captures both the timing of stress drops and the statistical distribution of slip magnitudes across stress regimes.

The dual-Poisson model effectively captures the complex behavior at low stresses, while the single-Poisson model accurately reflects the more discrete failure behavior at higher stresses.

In summary, the transition from dual- to single-Poisson dynamics across increasing normal stress is reflected not only in the inferred model structure but also in the empirical and simulated characteristics of fault behavior. At low normal stresses, frequent small slips and complex stress buildup patterns necessitate richer modeling. In contrast, at high normal stresses, failure becomes more discrete and catastrophic, and our simplified model still achieves strong agreement with data. These results reinforce the flexibility and physical interpretability of our stochastic inference framework across diverse experimental conditions.

3.4. **Growth Function Inference with ADAM-SINDy.** In order to experimentally infer the growth function g, we assume the model derived in the Appendix, Section 7.3:

$$\frac{d\mu}{dt} = -\frac{bV}{D_c} \sinh\left(\frac{\mu - \mu_0}{b} + \ln\left(\frac{1}{2} \cdot \left(\frac{V}{V_0}\right)^{1-\frac{a}{b}}\right)\right). \tag{3.1}$$

Although previous SDE inference models posited that g may be assumed to be linear [52] for certain physical systems such as cell size and division, we found that modeling g with a hyperbolic sine model was more appropriate for labquakes, apparent in Figure 5 and Figure 7 in Appendix, Section 7.3. Our approach helps us to gain insights on labquakes' characteristics: by inferring the coefficients α, β, and γ in $\frac{d\mu}{dt} = \alpha \sinh(\beta\mu + \gamma)$ (a form

suggested by Equation 3.1), we may learn about the values of slip velocity V and slip distance D_c.

Although previous literature has attempted the topic of inferring differential equations with certain nonlinear forms such as rational fractions [22], the inference of differential equations following sinh relations is not well-explored. SINDy [9] is a general method to infer ODE dynamical systems, involving the construction of a library $\boldsymbol{\Theta}$ of potential forms for the model and running a sparse regression to determine the coefficients $\boldsymbol{\Xi}$, using a sequential thresholded least-squares algorithm for minimal intractability. However, the pre-construction of $\boldsymbol{\Theta}$ is of limited efficacy for complex dynamical systems such as labquake friction.

Therefore, we infer the growth function g through harnessing the ADAM-SINDy approach. ADAM-SINDy [51] is a hybrid approach combining the traditional SINDy inference methodology with Adam optimization [21] in order to redress certain shortcomings. While standard SINDy assumes knowledge of a library of underlying forms for the differential equation being inferred, ADAM-SINDy can more flexibly adjust the inferred parameters, allowing it to dynamically infer many different nonlinear differential equations. For example, our growth function model for labquake friction is in the form of $\alpha \sinh(\beta\mu + \gamma)$, for some α, β, and γ. The standard SINDy approach would require prior knowledge of β and γ for $\sinh(\beta\mu + \gamma)$ to be part of the library of candidate models. Because this is unrealistic for complex experimental systems such as ours, ADAM-SINDy, which sets α, β, and γ as dynamic parameters, obviates this issue.

We applied the ADAM-SINDy approach to infer g on experimental data, again using the 11 MPa data from Marone's experiment `p4348` [23]. The approach yielded minimal loss ($6.680 \cdot 10^{-7}$ after 49,999 epochs), as seen in Figure 4.

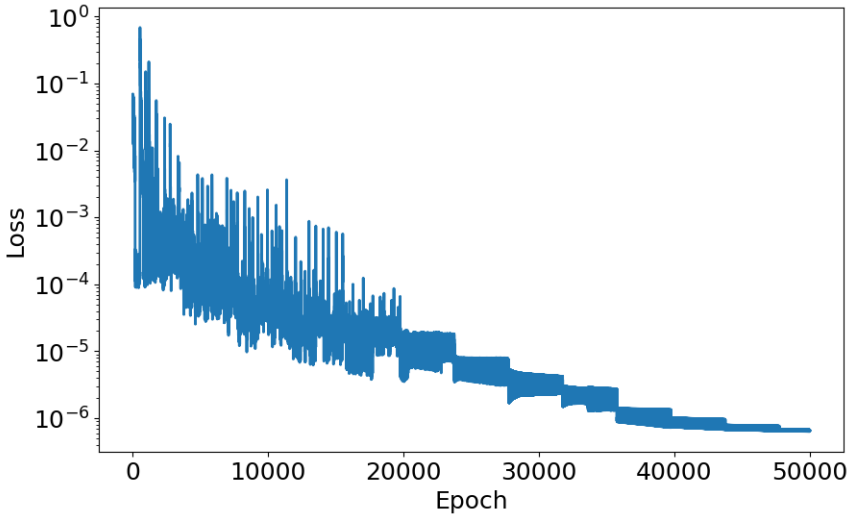

Figure 4. Plot of the loss to illustrate the efficacy of ADAM-SINDy with the 11 MPa data from experiment `p4348`.

After inferring α, β, and γ from the experimental data, we may use these values to gain insights on the constants in the frictional state growth through Equation 3.1. In particular, because we have

$$-\frac{bV}{D_c}\sinh\left(\frac{\mu-\mu_0}{b}+\ln\left(\frac{1}{2}\cdot\left(\frac{V}{V_0}\right)^{1-\frac{a}{b}}\right)\right)=\alpha\sinh(\beta\mu+\gamma),$$

we may derive constant $b=\frac{1}{\beta}$, $V=V_0\left(2e^{\gamma+\mu_0\beta}\right)^{\frac{1}{1-\alpha\beta}}$, and $D_c=-\frac{V_0\left(2e^{\gamma+\mu_0\beta}\right)^{\frac{1}{1-\alpha\beta}}}{\alpha\beta}$. Thus, the ADAM-SINDy framework applied to growth function inference is a novel method for understanding labquake friction through the slip velocity V and the characteristic slip distance D_c.

Moreover, understanding the form of the growth function allows us to update our SDE model, as detailed in Section 2.3, and obtain more informed results for λ and the overall frictional trajectory, reflected in Figure 1 (D) and Figure 5.

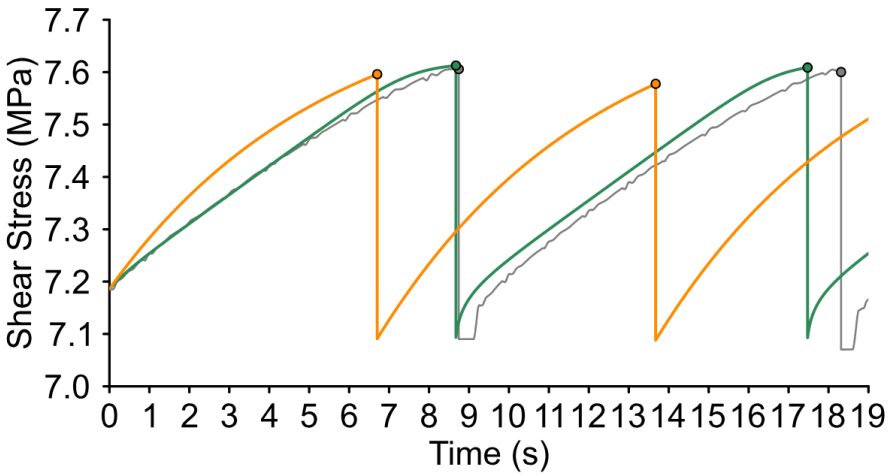

Figure 5. Plot of shear stress trajectories from data associated with `p4348` at 11 MPa (gray) and our simulations using the inferred linear (orange) and sinh (green) functions for fine-tuning.

4. Discussion & Conclusions

We have introduced a novel data-driven inference framework for analyzing laboratory earthquake dynamics, demonstrating that stochastic differential equation (SDE) inference can reconstruct both the continuous accumulation and the discontinuous release of shear stress. Unlike black-box machine learning approaches, our method provides interpretable governing equations that directly reflect the physical processes of stress growth and slip. A central novelty of this work is the discovery that the growth function $g(\mu)$ follows a hyperbolic sine relation. This sinh structure is important because it links laboratory observations to the Perrin–Rice–Zheng (PRZ) rate-and-state friction equation, which has been theoretically proposed but rarely validated directly from

data. By identifying this nonlinear behavior empirically, our inference framework offers a mechanistic explanation of labquake friction that bridges experiment and theory.

A second major innovation lies in extending standard SDE inference to incorporate two distinct Poisson processes, representing microslips and major slips. Previous SDE-based inference frameworks typically account for only a single Poisson-driven jump process. By introducing a dual-process formulation, our model captures the bimodal distribution of stress drops observed in labquake data, representing small precursory failures and large catastrophic slips as interdependent but distinct processes. This extension demonstrates how inference methods can be systematically generalized to handle increasingly complex stochastic jump systems, with labquakes providing a test case of direct geophysical importance.

Nevertheless, several limitations remain. While our results span a range of normal stresses, validation under different slip velocities and loading conditions is essential to fully assess generalizability.

In summary, our study demonstrates that stochastic inference offers a powerful and interpretable alternative to machine learning in analyzing labquake dynamics. By combining Bayesian inference, dual-Poisson process modeling, and sparse nonlinear discovery, we provide new insights into the governing laws of fault stress evolution. We anticipate that this framework can be generalized to a broad class of stochastic jump processes in geophysics and beyond.

5. Acknowledgments

The authors would like to thank the MIT PRIMES-USA program for their continual support of this research. We would also like to thank Jonathan Du for providing insights on ridge regression techniques, as well as Professor Amirhossein Arzani and his research group at the University of Utah for discussing the theory and implementation of ADAM-SINDy with us.

6. Bibliography

[1] Helen K. Alexander and R. Craig MacLean. Stochastic bacterial population dynamics restrict the establishment of antibiotic resistance from single cells. *Proceedings of the National Academy of Sciences*, 117(32):19455–19464, 2020.

[2] S. Derin Babacan, Martin Luessi, Rafael Molina, and Aggelos K. Katsaggelos. Sparse bayesian methods for low-rank matrix estimation. *IEEE Transactions on Signal Processing*, 60(8):3964–3977, Aug 2012.

[3] Pathikrit Bhattacharya, Allan M. Rubin, Elsa Bayart, Heather M. Savage, and Chris Marone. Critical evaluation of state evolution laws in rate and state friction: Fitting large velocity steps in simulated fault gouge with time-, slip-, and stress-dependent constitutive laws. *Journal of Geophysical Research: Solid Earth*, 120(9):6365–6385, 2015.

[4] Å. Björck. Numerics of gram-schmidt orthogonalization. *Linear Algebra and its Applications*, 197-198:297–316, 1994.

[5] M. L. Blanpied, T. E. Tullis, and J. D. Weeks. Frictional behavior of granite at low and high sliding velocities. *Geophysical Research Letters*, 14(5):554–557, 1987.

[6] W. F. Brace and J. D. Byerlee. Stick-slip as a mechanism for earthquakes. *Science*, 153(3739):990–992, 1966.

[7] W. F. Brace and J. D. Byerlee. California earthquakes: Why only shallow focus? *Science*, 168(3939):1573–1575, 1970.

[8] N. Brantut, A. Schubnel, J.-N. Rouzaud, F. Brunet, and T. Shimamoto. High-velocity frictional properties of a clay-bearing fault gouge and implications for earthquake mechanics. *Journal of Geophysical Research: Solid Earth*, 113(B10), 2008.

[9] Steven L. Brunton, Joshua L. Proctor, and J. Nathan Kutz. Discovering governing equations from data by sparse identification of nonlinear dynamical systems. *Proceedings of the National Academy of Sciences*, 113(15):3932–3937, 2016.

[10] J. Byerlee. Friction of rocks. *Pure and Applied Geophysics*, 116(4):615–626, 1978.

[11] James D. Byerlee. Frictional characteristics of granite under high confining pressure. *Journal of Geophysical Research (1896-1977)*, 72(14):3639–3648, 1967.

[12] R.G. Cowell, Alexander Dawid, Steffen Lauritzen, and David Spiegelhalter. *Probabilistic Networks and Expert Systems*, volume 43. 01 2001.

[13] James H. Dieterich. Time-dependent friction as a possible mechanism for aftershocks. *Journal of Geophysical Research (1896-1977)*, 77(20):3771–3781, 1972.

[14] James H. Dieterich. Modeling of rock friction: 1. experimental results and constitutive equations. *Journal of Geophysical Research: Solid Earth*, 84(B5):2161–2168, 1979.

[15] James H. Dieterich. Potential for geophysical experiments in large scale tests. *Geophysical Research Letters*, 8(7):653–656, 1981.

[16] Chuong B. Do and Serafim Batzoglou. What is the expectation maximization algorithm? *Nature Biotechnology*, 26:897–899, 2008.

[17] A. Gualandi, D. Faranda, C. Marone, M. Cocco, and G. Mengaldo. Deterministic and stochastic chaos characterize laboratory earthquakes. *Earth and Planetary Science Letters*, 604:117995, 2023.

[18] Stephen Hickman, Richard Sibson, and Ronald Bruhn. Introduction to special section: Mechanical involvement of fluids in faulting. *Journal of Geophysical Research: Solid Earth*, 100(B7):12831–12840, 1995.

[19] P. A. Johnson, B. Ferdowsi, B. M. Kaproth, M. Scuderi, M. Griffa, J. Carmeliet, R. A. Guyer, P-Y. Le Bas, D. T. Trugman, and C. Marone. Acoustic emission and microslip precursors to stick-slip failure in sheared granular material. *Geophysical Research Letters*, 40(21):5627–5631, 2013.

[20] H. Kanamori. Mechanics of earthquakes. *Annual Review of Earth and Planetary Sciences*, 22(Volume 22, 1994):207–237, 1994.

[21] Diederik P. Kingma and Jimmy Ba. Adam: A method for stochastic optimization. *arXiv [Preprint]*, 2017. https://arxiv.org/abs/1412.6980.

[22] Niall M. Mangan, Steven L. Brunton, Joshua L. Proctor, and J. Nathan Kutz. Inferring biological networks by sparse identification of nonlinear dynamics. *IEEE Transactions on Molecular, Biological, and Multi-Scale Communications*, 2(1):52–63, 2016.

[23] Chris Marone. Marone lab data. http://psudata.s3-website.us-east-2.amazonaws.com/.

[24] Chris Marone. Laboratory-derived friction laws and their application to seismic faulting. *Annual Review of Earth and Planetary Sciences*, 26(Volume 26, 1998):643–696, 1998.

[25] Charles W. Mase and Leslie Smith. Effects of frictional heating on the thermal, hydrologic, and mechanical response of a fault. *Journal of Geophysical Research: Solid Earth*, 92(B7):6249–6272, 1987.

[26] Gregory C. McLaskey and Steven D. Glaser. Micromechanics of asperity rupture during laboratory stick slip experiments. *Geophysical Research Letters*, 38(12), 2011.

[27] T.K. Moon. The expectation-maximization algorithm. *IEEE Signal Processing Magazine*, 13(6):47–60, Nov 1996.

[28] André Niemeijer, Chris Marone, and Derek Elsworth. Frictional strength and strain weakening in simulated fault gouge: Competition between geometrical weakening and chemical strengthening. *Journal of Geophysical Research: Solid Earth*, 115(B10), 2010.

[29] Mitiyasu Ohnaka. Experimental studies of stick-slip and their application to the earthquake source mechanism. *Journal of Physics of the Earth*, 21(3):285–303, 1973.

[30] Judea Pearl. Chapter 2 - bayesian inference. In Judea Pearl, editor, *Probabilistic*

Reasoning in Intelligent Systems, pages 29–75. Morgan Kaufmann, San Francisco (CA), 1988.

[31] Gilles Perrin, James R. Rice, and Gutuan Zheng. Self-healing slip pulse on a frictional surface. *Journal of the Mechanics and Physics of Solids*, 43(9):1461–1495, 1995.

[32] J. R. Rice and A. L. Ruina. Stability of steady frictional slipping. *Journal of Applied Mechanics*, 50(2):343–349, 06 1983.

[33] James R. Rice. Constitutive relations for fault slip and earthquake instabilities. *Pure and Applied Geophysics*, 121(3):443–475, 1983.

[34] Keith Richards-Dinger and James H. Dieterich. Rsqsim earthquake simulator. *Seismological Research Letters*, 83(6):983–990, 11 2012.

[35] J. Rivière, Z. Lv, P.A. Johnson, and C. Marone. Evolution of b-value during the seismic cycle: Insights from laboratory experiments on simulated faults. *Earth and Planetary Science Letters*, 482:407–413, 2018.

[36] Bertrand Rouet-Leduc, Claudia Hulbert, David C. Bolton, Christopher X. Ren, Jacques Riviere, Chris Marone, Robert A. Guyer, and Paul A. Johnson. Estimating fault friction from seismic signals in the laboratory. *Geophysical Research Letters*, 45(3):1321–1329, 2018.

[37] Bertrand Rouet-Leduc, Claudia Hulbert, Nicholas Lubbers, Kipton Barros, Colin J. Humphreys, and Paul A. Johnson. Machine learning predicts laboratory earthquakes. *Geophysical Research Letters*, 44(18):9276–9282, 2017.

[38] Samuel H. Rudy, Steven L. Brunton, Joshua L. Proctor, and J. Nathan Kutz. Data-driven discovery of partial differential equations. *Science Advances*, 3(4):e1602614, 2017.

[39] Andy Ruina. Slip instability and state variable friction laws. *Journal of Geophysical Research: Solid Earth*, 88(B12):10359–10370, 1983.

[40] C. H. Scholz. Microfracturing and the inelastic deformation of rock in compression. *Journal of Geophysical Research (1896-1977)*, 73(4):1417–1432, 1968.

[41] C. H. Scholz. The critical slip distance for seismic faulting. *Nature*, 336(6201):761–763, 1988.

[42] C H Scholz. Mechanics of faulting. *Annual Review of Earth and Planetary Sciences*, 17(Volume 17, 1989):309–334, 1989.

[43] C. H. Scholz and J. Campos. On the mechanism of seismic decoupling and back arc spreading at subduction zones. *Journal of Geophysical Research: Solid Earth*, 100(B11):22103–22115, 1995.

[44] Christopher H. Scholz. Static fatigue of quartz. *Journal of Geophysical Research (1896-1977)*, 77(11):2104–2114, 1972.

[45] Christopher H. Scholz. *The Mechanics of Earthquakes and Faulting*. Cambridge University Press, 2 edition, 2002.

[46] Michael Schöniger and Arndt Von Haeseler. A stochastic model for the evolution

of autocorrelated dna sequences. *Molecular Phylogenetics and Evolution*, 3(3):240–247, 1994.

[47] Marco M. Scuderi, Brett M. Carpenter, and Chris Marone. Physicochemical processes of frictional healing: Effects of water on stick-slip stress drop and friction of granular fault gouge. *Journal of Geophysical Research: Solid Earth*, 119(5):4090–4105, 2014.

[48] Paul Segall and James R. Rice. Dilatancy, compaction, and slip instability of a fluid-infiltrated fault. *Journal of Geophysical Research: Solid Earth*, 100(B11):22155–22171, 1995.

[49] R. M. Stesky. Rock friction-effect of confining pressure, temperature, and pore pressure. *Pure and Applied Geophysics*, 116(4):690–704, 1978.

[50] John Townend. *What Do Faults Feel? Observational Constraints on the Stresses Acting On Seismogenic Faults*, pages 313–327. American Geophysical Union (AGU), 2006.

[51] Siva Viknesh, Younes Tatari, and Amirhossein Arzani. Adam-sindy: An efficient optimization framework for parameterized nonlinear dynamical system identification. *arXiv [Preprint]*, 2025. https://arxiv.org/abs/2410.16528.

[52] Shijie Zhang, Chenyi Fei, and Jörn Dunkel. Nonlinear memory in cell division dynamics across species. *arXiv [Preprint]*, 2024. https://arxiv.org/abs/2408.14564.

[53] Ying Zhang, Congcong Wen, Chengxiang Zhan, and Didier Sornette. Integrating artificial intelligence and geophysical insights for earthquake forecasting: A cross-disciplinary review. *Earth-Science Reviews*, 270:105232, 2025.

[54] Mark D. Zoback and Mary Lou Zoback. Tectonic stress field of north america and relative plate motions. In *Neotectonics of North America*. Geological Society of America, 01 1991.

7. Appendix

7.1. **Bayesian Inference.** In order to find $P(\mathbf{w}|s_t)$ and ultimately $\lambda(s_t, s_t^*)$, of interest to us is how $P(\mathbf{w}|s_t)$ is proportional to the product of $P(s_t|\mathbf{w})$ and $P(\mathbf{w})$. We work with an inhomogeneous Poisson process, namely $\mathscr{N}_t$, so we have

$$P(s_t|\mathbf{w}) = e^{-\int \lambda(s_t, s_t^*)dt} \prod_i \lambda\left(s_{\tau_i}, s^*_{\tau_i}\right).$$

Then, we use sparse Bayesian inference [2, 12, 30] to estimate $P(\mathbf{w})$:

$$P(\mathbf{w}) \propto \prod_{i,j} e^{-\frac{\mathbf{w}_{ij}^2}{2\boldsymbol{\sigma}_{ij}^2}},$$

where $\boldsymbol{\sigma}_{ij}$ control sparsity. Namely, the smaller $\boldsymbol{\sigma}_{ij}$ is, the closer $\mathbf{w}_{ij}$ becomes to zero, which promotes sparsity in $\mathbf{w}$. Note that $\boldsymbol{\sigma}_{ij}$ are estimated through the Expectation-Maximation algorithm [16, 27]. From these $\boldsymbol{\sigma}_{ij}$ values, we may calculate $\hat{\mathbf{w}}$ and then obtain $\lambda(s_t, s_t^*)$ from Equation (2.3).

We consider that $\text{BIC} = \ln P(s_t|\hat{\mathbf{w}}) - \frac{1}{2}\ln|\hat{\mathbf{H}}|$, where $\hat{\mathbf{H}}$ is the Hessian of $\ln P(s_t|\hat{\mathbf{w}})$. The term including $\ln|\hat{\mathbf{H}}|$ penalizes candidate models with a large number of parameters, encouraging sparsity. Therefore, the candidate model with the largest BIC is considered the most parsimonious.

7.2. **Bimodality of Slip Sizes in Frictional States.** We motivate our splitting of the Poisson processes in modeling the frictional states of experiments with low normal stress because of the slip sizes' bimodality, as evident in Figure 6. Across experimental

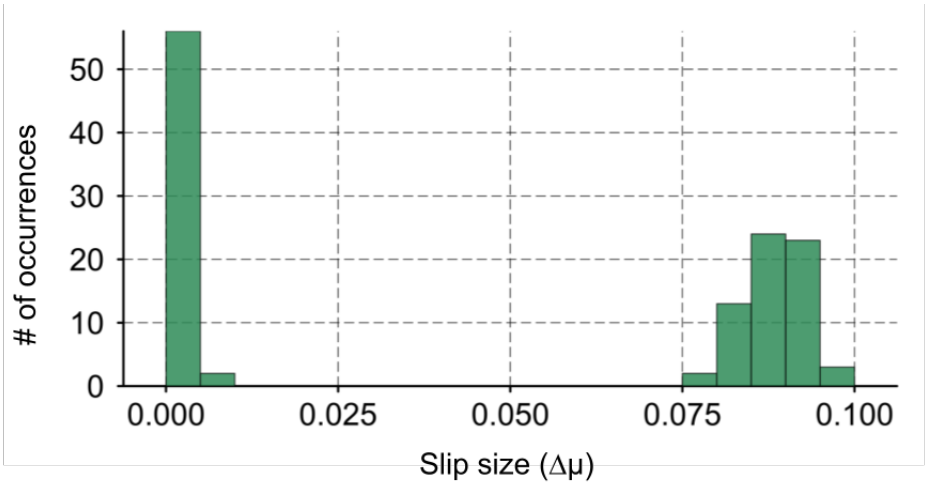

Figure 6. Labquake data shows a characteristic bimodal distribution of friction state slip sizes, indicating that two separate yet mutually influencing processes are responsible for stress evolution over time.

data, this bimodality may be split between microslips ($\Delta\mu < 0.4$) and major slips ($\Delta\mu > 0.4$).

7.3. **Growth Function Derivation.** The rate-and-state friction equation 2.1 referenced in Section 2.1 evaluates the friction constant μ at a given state. However, we wish to glean insights into its instantaneous growth in order to understand the time evolution of the labquake system.

The rate-and-state friction equation may be rewritten as follows:

$$\mu - \mu_0 = \ln\left(\frac{V^a \cdot V_0^b \cdot \theta^b}{V_0^a \cdot D_c^b},\right)$$

$$e^{\mu-\mu_0} = \frac{V^a \cdot V_0^{b-a}}{D_c^b} \cdot \theta^b,$$

$$\theta = \frac{D_c}{V^{\frac{a}{b}} \cdot V_0^{1-\frac{a}{b}}} \cdot e^{\frac{\mu-\mu_0}{b}}.$$

Additionally, we can find from the rate-and-state friction equation that

$$d\mu = \frac{b}{\theta} d\theta.$$

The exact mechanics and dynamics of the evolution of the state variable θ over time is the subject of contentious debate [24]. There are three primary theories for the time-evolution dynamics of θ, leading to three versions of the rate-and-state law.

First, the Dieterich (aging) law [14] describes the evolution of θ as:

$$\frac{d\theta}{dt} = 1 - \frac{V\theta}{D_c}.$$

Thus, in the Dieterich theory, friction continuously increases due to time-dependent strengthening of asperity contacts, even when the faults remain stationary ($V = 0$).

In contrast, the Ruina (slip) law [39] is given by the following:

$$\frac{d\theta}{dt} = -\frac{V\theta}{D_c} \ln\left(\frac{V\theta}{D_c}\right).$$

In the Ruina theory, the friction variable θ only grows when fault slip occurs ($V \neq 0$).

Finally, the third theory by Perrin, Rice, and Zheng (PRZ) [31],

$$\frac{d\theta}{dt} = 1 - \left(\frac{V\theta}{2D_c}\right)^2,$$

incorporates both aging and slip-dependent behaviors, leading to a more symmetrical response to velocity perturbations.

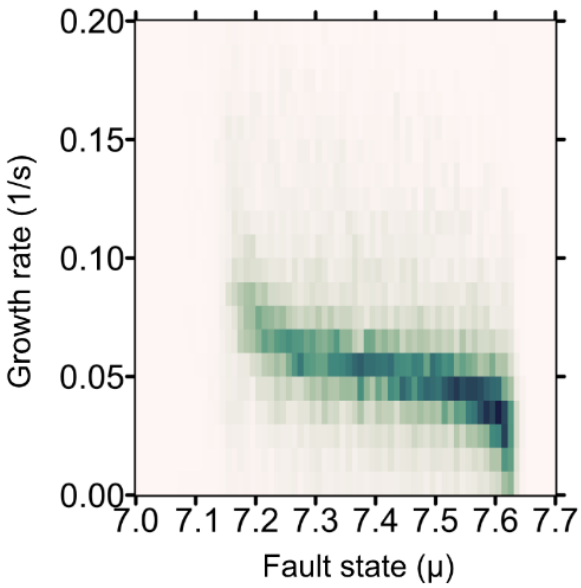

Figure 7. Heatmap of frictional state μ versus growth rate g from the 11 MPa data in Marone's experiment p4348. In the experimental data, g follows a $\sinh \mu$ relation.

Using the Dieterich, Ruina, and PRZ theories, we predict the dynamics of μ as follows:

$$\text{Dieterich: } \frac{d\mu}{dt} = \frac{b}{\theta} \cdot \frac{d\theta}{dt} = \frac{b}{\theta}\left(1 - \frac{V\theta}{D_c}\right).$$

$$\text{Ruina: } \frac{d\mu}{dt} = \frac{b}{\theta} \cdot \frac{d\theta}{dt} = \frac{b}{\theta}\left(-\frac{V\theta}{D_c}\ln\left(\frac{V\theta}{D_c}\right)\right).$$

$$\text{PRZ: } \frac{d\mu}{dt} = \frac{b}{\theta} \cdot \frac{d\theta}{dt} = \frac{b}{\theta}\left(1 - \left(\frac{V\theta}{2D_c}\right)^2\right).$$

Combining our expression for θ from the rate-and-state friction equation with the Dieterich, Ruina, and PRZ laws, we may derive the following equations for μ's dynamics:

$$\text{Dieterich: } \frac{d\mu}{dt} = \frac{bV}{D_c}\left(\left(\frac{V_0}{V}\right)^{1-\frac{a}{b}} \cdot e^{\frac{-\mu+\mu_0}{b}} - 1\right).$$

$$\text{Ruina: } \frac{d\mu}{dt} = -\frac{bV}{D_c}\left(\frac{\mu-\mu_0}{b} + \ln\left(\frac{V}{V_0}\right)^{1-\frac{a}{b}}\right).$$

$$\text{PRZ: } \frac{d\mu}{dt} = -\frac{bV}{D_c}\sinh\left(\frac{\mu-\mu_0}{b} + \ln\left(\frac{1}{2}\cdot\left(\frac{V}{V_0}\right)^{1-\frac{a}{b}}\right)\right).$$

As explained in Section 2.3, we may think of the growth function g as being $\frac{d\mu}{dt}$. Thus, Dieterich predicts that g will follow a $e^{-\mu}$ relation, and Ruina predicts a relation linear in μ. We note that PRZ predicts that g will follow a $\sinh \mu$ relation, which we corroborate with our experimental data. For example, we used the 11 MPa data from Marone's experiment p4348 [23] to infer growth function g and see how it changes depending on the frictional state μ, as seen in Figure 7. As evident from the figure, the growth function g follows a $\sinh \mu$ relation.

The Harker School, San Jose, CA 95129, USA
Email address: jessicashanahu@gmail.com

Chantilly High School, Chantilly, VA 20151, USA
Email address: me@aryanraj.xyz

Massachusetts Institute of Technology, Cambridge, MA 02139, USA
Email address: shjzhang@mit.edu